

Post-Treatment Engineering of Vacuum-Deposited Cs2NaBil6 Double Perovskite Film for Enhanced Photovoltaic Performance

Peizhou Li, Weiyin Gao,* Chenxin Ran, Hua Dong, Xun Hou, and Zhaoxin Wu*

Lead-free double perovskite materials have recently shown promising in optoelectronic application. However, the poor solubility of these materials makes them difficult to form a high-quality thin film via the solution-processible technology, which leads to the poor photovoltaic performance of a solar cell device. Herein, the vacuum-evaporated Cs2NaBil6 double perovskite film with high quality achieved by the post-treatment engineering is demonstrated. It is found that soaking in isopropyl alcohol (IPA) followed by annealing in dimethyl formamide (DMF) atmosphere can enlarge the size of grains, lower trap-state density, and remove side product of the Cs2NaBil6 film. The resulting solar cell devices show a power conversion efficiency (PCE) of 0.21% ($V_{\rm OC} = 0.70 \, \text{V}$, $I_{SC} = 0.91 \text{ mA cm}^{-2}$, and fill factor (FF) = 33%), which is tenfold higher than the control device without post-treatment (PCE = 0.02%, $V_{\rm OC}$ = 0.49 V, $I_{SC} = 0.19 \text{ mA cm}^{-2}$, and FF = 24%). In addition, the device shows robust stability against moisture and oxygen in ambient condition. The vacuum deposition method accompanied with a post-treatment strategy, in this work, provides an important research direction in improving the quality of a double perovskite film and the PCE of corresponding perovskite solar cells (PSCs).

1. Introduction

The research of a thin-film photovoltaic device based on a hybrid organic-inorganic lead (Pb) halide perovskite material has been significantly progressed during the last decade, and the world record power conversion efficiency (PCE) has recently reached 24.2%. [1-6] The promising performance of perovskite solar cells (PSCs) is already competitive with CdTe and polycrystalline silicon-based solar cells. [7] Despite the rapid development of PSCs,

Key Laboratory of Photonics Technology for Information Key Laboratory for Physical Electronics and Devices of the Ministry of Education School of Electronic and Information Engineering Xi'an Jiaotong University

P. Li, Dr. W. Gao, Dr. C. Ran, Dr. H. Dong, Prof. X. Hou, Prof. Z. Wu

Xi'an 710049, P. R. China

E-mail: weiyin_gao@mail.xjtu.edu.cn; zhaoxinwu@mail.xjtu.edu.cn

Dr. C. Ran, Dr. H. Dong, Prof. Z. Wu

Collaborative Innovation Center of Extreme Optics Shanxi University

Taiyuan 030006, P. R. China

The ORCID identification number(s) for the author(s) of this article can be found under https://doi.org/10.1002/pssa.201900567.

DOI: 10.1002/pssa.201900567

the instability and the toxicity of a classical Pb-based perovskite material remain the potential risks for its large-scale commercial application. [8–10] As a result, much effort has been made on exploring lead-free perovskite materials with high stability and, meanwhile, low toxicity.[11,12]

Substitution of Pb²⁺ by Sn²⁺ or Ge²⁺, which are in the same IV main group with Pb²⁺ in the periodic table, has been studied since 2014. Notably, Sn-based PSC devices have recently shown promising PCE approaching 10%.[13-15] Nevertheless. the easy oxidization of Sn²⁺ to Sn⁴⁺ and Ge^{2+} to Ge^{4+} leads to the instability of PSC devices in ambient condition, which remains the biggest challenge in Sn- or Ge-based PSCs. $^{[16-20]}$ In addition to Sn or Ge, another candidate for the substitution of Pb2+ is non-toxic Bi3+ and Sb3+ in the V main group, but their corresponding 0D or 2D A₃B₂X₉ crystal structure tends to strongly bound excitons, leading to low charge mobility and inferior

photovoltaic performance.[21]

Recently, researchers have shown great interest in lead-free double perovskite materials, which possess a crystal structure of elpasolite with a formula of A₂BB'X₆. Such types of quaternary halides are formed by replacing two Pb2+ cations with a monovalent B⁺ metal cation and another trivalent B'³⁺ metal cation, keeping the total number of valence electrons and 3D geometry unchanged compared with the ABX₃ structure.^[22] Although a large amount of B⁺ and B'³⁺ candidates can be selected to form a double perovskite structure, [23] only some of them fit the properties that are required for an effective light absorber material, including suitable decomposition enthalpy (ΔH), suitable band structure, small effective carrier masses, and low exciton binding energy.^[24] In the past three years, the synthesis of some double perovskites has been reported, such as Cs2AgBiX6 (X = Cl, Br), (25) $Cs_2AgSbCl_6$, $Cs_2AgInCl_6$, (26) $(MA)_2AgBiBr_6$, (27) $(MA)_2KBiCl_6$, (28) $(MA)_2TlBiBr_6$, (29) and Cs_2NaBil_6 . (30) However, only Cs2AgBiBr6 and Cs2NaBiI6 are reported to successfully apply into a solar cell device. Using a spin-coating film-forming method, PSCs based on Cs2AgBiBr6 and Cs2NaBiI6 films show a PCE of 2.5% and 0.42%, respectively. These low PCEs are owing to the poor quality of the double perovskite film made from the solution process. One reason is the low solubility of double perovskite materials in conventional polar solvent. For example,

18626319, 2019, 23, Downloaded from https://onlinelibrary.wiley.com/doi/10.1002/pss.20.1900567 by CAS-XIAN INSTITUTION OPTICS PRECISION MECHANICS, Wiley Online Library on [10/11/2025]. See the Terms

on Wiley Online Library for rules of use; OA articles are governed by the applicable Creative Commons License

the maximum solubility of $Cs_2AgBiBr_6$ in dimethylsulfoxide (DMSO) is less than $0.4\,\rm M$, and the maximum solubility of Cs_2NaBiI_6 in dimethyl formamide (DMF) is only 1 mg mL⁻¹. In addition to the low solubility, the double perovskite materials also show fast crystallization rate during the spin-coating process, which results in poor film morphology with holes and rough surface. Therefore, the low solubility and fast crystallization rate of double perovskite materials hinder the realization of the high-quality thin film, leading to their poor photovoltaic performance.

To avoid the drawbacks of the solution-processed double perovskite film, the vacuum deposition technology is a better choice. For example, Liu and co-workers demonstrated a sequential-vapor-deposition procedure to fabricate the $Cs_2AgBiBr_6$ film, and a PCE of $\approx\!1.4\%$ can be achieved. The advantages of vacuum deposition technology are 1) facile tenability of film thickness; 2) homogeneous film quality on large-scale area; and 3) high reproducibility. However, the vacuum-deposited film may suffer from the presence of side products, high density of grain boundaries (GBs), and small grain size of the film. $^{[35-37]}$ These disadvantages could largely limit the photovoltaic properties of the double perovskite film.

In this work, the Cs_2NaBiI_6 film is deposited by the vacuum-deposited method, and post-treatment engineering is then applied to improve the quality of the Cs_2NaBiI_6 film. Post-treatment processes are found to eliminate the side product, enlarge the grain size, and lower the defect density of the as-evaporated Cs_2NaBiI_6 film. The photovoltaic performance can be correspondingly enhanced by tenfold (from 0.02% to 0.21%) after optimizing the parameters of post-treatment processes. Moreover, the PSC device shows no PCE loss after stored in ambient condition for 100 day.

2. Results and Discussion

Prior to vacuum deposition of the Cs_2NaBiI_6 film, Cs_2NaBiI_6 powder was synthesized through a simple one-step hydrothermal process. Figure 1a shows the crystal structure of Cs_2NaBiI_6 , which shows a typical 3D perovskite structure with corner-shared AgI_6 and BiI_6 octahedral alternatively in all three directions. The as-prepared powder shows small crystals with dark orange color (Figure 1b). The scanning electron microscopy (SEM) image in Figure 1c shows the typical 3D structure of Cs_2NaBiI_6 particles

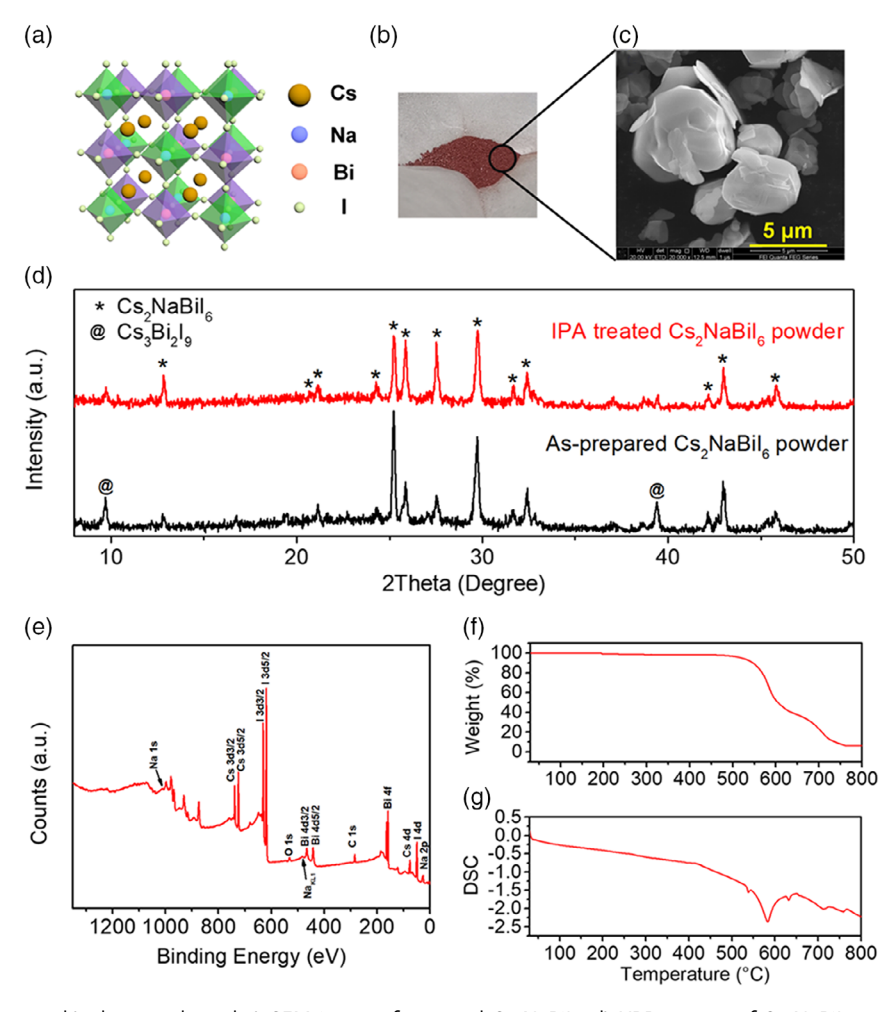


Figure 1. a) Crystal structure, b) photograph, and c) SEM image of prepared Cs_2NaBil_6 . d) XRD pattern of Cs_2NaBil_6 powder before and after IPA treatment. e) XPS, f) TGA, and g) DSC characterization of Cs_2NaBil_6 powder.



www.advancedsciencenews.com



with smooth surfaces. The X-ray diffraction (XRD) pattern in Figure 1d demonstrates the diffraction peaks of Cs_2NaBiI_6 at 2θ of 12.82°, 21.14°, 24.28°, 25.22°, 25.86°, 27.52°, 29.74°, 31.68°, 32.40°, 42.18°, 42.98°, and 45.78°, which are in agreement with the literature. [30] The diffraction peaks at 2θ of 9.72° and 39.46° are due to the presence of trace amount of Cs₃Bi₂I₉ side product, which is due to the decomposition of Cs2NaBiI6 during the cooling period of the chemical synthesis process.^[30] Because isopropyl alcohol (IPA) is reported to be effective in removing the adsorbed chemical-induced surface states on Cs₂AgBiBr₆ double perovskite, we tried to treat the Cs₂NaBiI₆ powder with IPA. The treatment was carried out by continuous stirring of Cs2NaBiI6 powder in IPA for 1 h under room temperature. It can be observed in XRD results that after IPA treatment, the intensities of peaks at 2θ of 9.72° and 39.46° are obviously reduced, indicating that IPA is valid in removing side product and purifying the Cs2NaBiI6 material. The full range X-ray photoelectron spectroscopy (XPS) measurement of Cs₂NaBiI₆ powder is shown in Figure 1e, which displays the presence of all four elements (Na, Bi, Cs, and I) in Cs2NaBiI6. It is worth noting that a Na_{KL1} Auger peak located at \approx 497 eV can be observed, revealing the existence of ionic sodium rather than sodium oxides. This is because for Na⁺, 1s peak and Auger peak are always simultaneously observed in the XPS spectra. [38] The narrow spectra of Cs 3d, Na 1s, Bi 4f, and I 3d (Figure S1, Supporting Information) all fit well standard binding energy differences of each element with ion valences of 1⁺, 1⁺, 3⁺, and 1⁻, respectively.^[30] Moreover, the thermal stability of Cs₂NaBiI₆ is studied by thermo gravimetric analyzer (TGA) and differential scanning calorimeter (DSC) measurements. It is observed that Cs₂NaBiI₆ begins to lose weight at 500 °C, implying its thermal stability as high as 500 °C (Figure 1f). More importantly, no DSC peak is observed when temperature is <500 °C (Figure 1g), demonstrating no phase transition occurring in this temperature range.

Figure 2a shows the illustration of the whole process of film fabrication in this work, including the vacuum evaporation deposition of the Cs₂NaBiI₆ film and post-treatment of the as-evaporated Cs2NaBiI6 film. In particular, the Cs2NaBiI6 film is first thermally evaporated on the SnO₂:F/compact TiO₂ (c-TiO₂) substrate under vacuum ($<10^{-3}$ pa). Thereafter, the film undergoes three different post-treatment paths in N₂-filled glove box. As shown in Figure 2a, Path 1 contains two stages of annealing at 150 °C first and then 210 °C (namely, "No treatment"). Path 2 introduces DMF atmosphere during the first annealing stage at 150 °C, and then 210 °C in N2 (namely, "DMF"). Path 3 further introduces IPA soaking step before annealing in DMF atmosphere (namely, "IPA + DMF"). From the SEM images of the Cs₂NaBiI₆ film following different paths, significant surface morphology change can be observed (Figure 2b-e). The morphology of the as-evaporated Cs₂NaBiI₆ film is composed of small grains with many distinct holes between them (Figure 2b). Following Path 1, negligible morphology changing can be observed on the film morphology, indicating that the thermal energy could not promote the reconstruction of Cs2NaBiI6 grains. When following Path 2, holes between Cs2NaBiI6 grains are obviously eliminated, whereas the size of the grain shows little change, suggesting that the trace amount of DMF atmosphere could partially dissolve the surface of Cs2NaBiI6 grains, thus resulting in decomposition and recrystallization. The recrystallization will grow with undissolved large particles as nuclei and promote the joint growth of the grains, thus reducing GBs and defects and further improving the morphology of the film to some extent. However, this reconstruction of Cs₂NaBil₆ particles has limited impact on the grain size enlargement because the solubility of Cs2NaBiI6 is low in DMF as mentioned in the Introduction Section. Interestingly, by following Path 3, significantly enlarged grain size with neat grain surface of the Cs₂NaBiI₆ film is observed (Figure 2f). The key role of IPA on the double perovskite material has been observed in our previous work, which showed that using IPA as antisolvent, a high-quality Cs2AgBiBr6 double perovskite film with enlarged grain size can be obtained due to reconstruction and coarsening of Cs₂AgBiBr₆ grains. [31,39] In addition, from the XRD patterns of Cs₂NaBiI₆ after different post-treatment (Figure 2g), it can be observed that diffraction peaks of Cs₂NaBiI₆ are enhanced after IPA + DMF treatment. This result demonstrates that IPA could remove the side product and purify the Cs2NaBiI6 film, which is consistent with the result in Cs₂NaBiI₆ powder (Figure 1d). Figure 2h shows the morphology evolution after IPA + DMF treatment. Soaking in IPA leads to Ostwald ripening and coarsening of Cs2NaBiI6 grains resulting in enlarged size of the grains, and further annealing in DMF further improves the morphology of the film.

Furthermore, we investigated the impact of the post-treatment process on the electronic and optical properties of the Cs₂NaBiI₆ film. Space charge limited currents was carried out to measure the density of trap state in electron-only devices (FTO/c-TiO₂/ Cs₂NaBiI₆/Ag) of different Cs₂NaBiI₆ films. [40] As shown in Figure 3a, the onset voltage of the trap-filled limit (V_{TFL}) of the Cs2NaBiI6 film with no treatment is 1.01 V, which gives a trap-state density of $9.25 \times 10^{15} \, \text{cm}^{-3}$ (calculation details can be found in the Experimental Section in the Supporting Information). After introducing solvent annealing in DMF, the value of V_{TFI} decreases to 0.70 V, referring to a decreased trap-state density of 6.41×10^{15} cm⁻³. Further adding IPA soaking process prior to DMF atmosphere annealing leads to the value V_{TFL} of 0.61 V, corresponding to a trap-state density of $5.59 \times 10^{15}\,\text{cm}^{-3}$. These results confirm that the post-treatment processes effectively remove the surface states of the film. The optical property of Cs2NaBil6 films was characterized by UV-vis and photoluminescence (PL) spectra, as shown in Figure 3b. It should be noted that the Cs₂NaBiI₆ film with no treatment shows higher intensity in the range of 550-650 nm, which is due to the light scattering effect of rough morphology of the film in the presence of holes.^[41] After introducing IPA soaking and DMF annealing, the typical exciton absorption peak of Cs_2NaBiI_6 at ≈ 500 nm is enhanced. Similarly, the PL spectra of Cs₂NaBiI₆ with no treatment show no exciton emission peak, but an enhanced exciton emission peak at ≈550 nm after posttreatment can be observed after post-treatment, which is in agreement with the UV-vis spectra. These changes before and after post-treatment indicate that the post-treatment process could promote the phase purification of the Cs2NaBiI6 film. Furthermore, the bandgap of the Cs₂NaBiI₆ film is estimated. The Tauc plot in the direct mode delivers an estimated direct bandgap of 2.36 eV (Figure S2a, Supporting Information), which is in accordance with the calculated value (2.42 eV) reported in the literature. [24] However, the theoretical result indicates the indirect band nature of the Cs2NaBiI6 material. Therefore, fitting

18626319, 2019, 23, Downloaded from https://onlinelibrary.wiley.com/doi/10.1002/pssa.201900567 by CAS-XIAN INSTITUTION OPTICS PRECISION MECHANICS, Wiley Online Library on [1011/2025]. See the Terns

onditions) on Wiley Online Library for rules of use; OA articles are governed by the applicable Creative Commons License

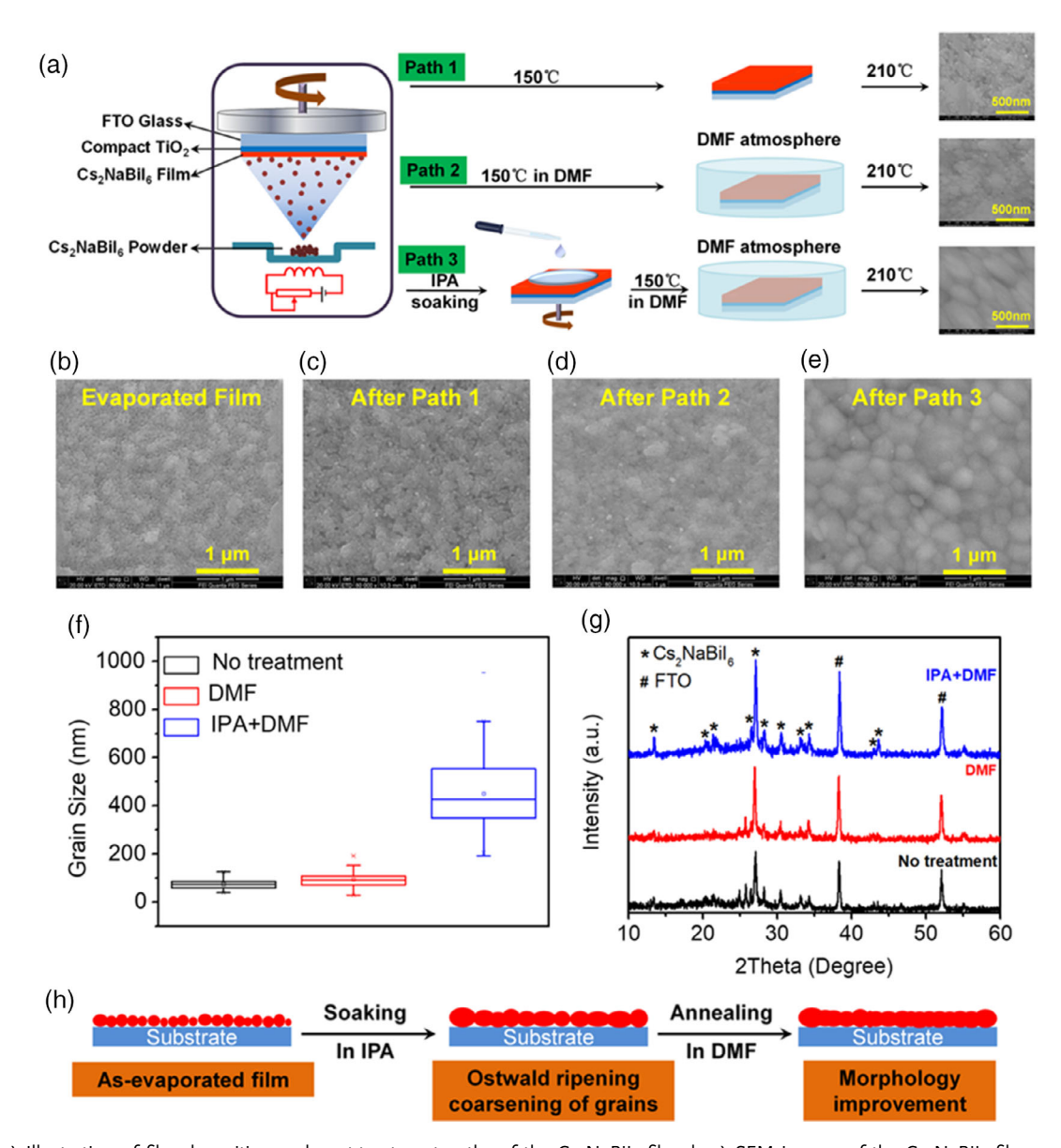


Figure 2. a) Illustration of film deposition and post-treatment paths of the Cs_2NaBil_6 film. b–e) SEM images of the Cs_2NaBil_6 film under different post-treatment paths. f) Grain size distribution and g) XRD pattern of the Cs_2NaBil_6 film under different post-treatment paths. h) Schematic showing the effect of post-treatment on the morphology of the Cs_2NaBil_6 film.

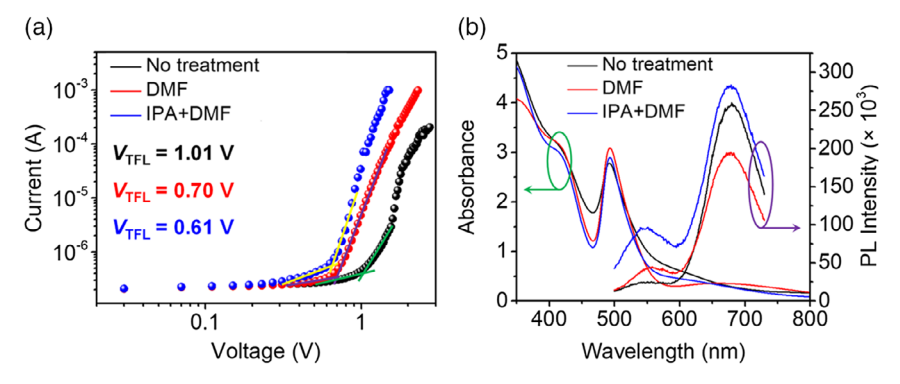


Figure 3. Characterizations of a) electrical and b) optical properties of the Cs2NaBil6 film under different post-treatment paths.

solidi September 1

by an indirect mode, the Tauc plot of the Cs_2NaBiI_6 film (Figure S2a, Supporting Information) suggests the phonon-assisted processes of indirect semiconductor, and the transitions at 1.52 and 2.10 eV occur with absorption and emission of a phonon, respectively. [42] Also, the indirect bandgap of 1.81 eV with an assisting phonon energy of 0.29 eV can be estimated. This value of 1.81 eV is in agreement with the PL results showing a PL emission peak at 675 nm (1.83 eV) (Figure 3b).

To study the photovoltaic performance, the PSC devices based on Cs2NaBiI6 films were fabricated in a normal device structure of Glass/FTO/c-TiO2/Cs2NaBiI6/Spiro-OMeTAD/Ag (Figure 4a). Figure 4b shows the cross-sectional SEM image of the device, and the thickness of the Cs2NaBiI6 layer is estimated to be \approx 300 nm. The ultroviolet photoelectron spectrometer (UPS) was used to measure the band structure of the Cs₂NaBiI₆ layer (Figure S3, Supporting Information). Combining the UPS result with the indirect bandgap of 1.81 eV estimated from PL spectra (Figure 3b), the valence band and conduction band of the Cs_2NaBiI_6 layer are located at -5.37and $-3.56\,\text{eV}$, respectively (Figure 4c). From J-V curves of Cs₂NaBiI₆ films with different post-treatment paths (Figure 4d), it can be seen that all the parameters (J_{SC}, V_{OC}, fill factor (FF), and PCE) increase after IPA soaking and DMF annealing, which is owing to the improved film quality after post-treatment as investigated earlier. The external quantum efficiency (EQE) spectra in Figure 4e show the enhanced photocurrent response in the range of 300-530 nm after post-treatment, revealing the higher photocharge collection after post-treatment. The PSC devices show some hysteresis effect (Figure 4f), which is always observed in the normal PSC devices owing to the charge traps at the TiO₂/perovskite interface. [43] Figure 5 shows the statistics of the photovoltaic parameter distributions of PSCs based on different Cs2NaBiI6 films, and the post-treatment clearly enhances

every parameter of the device. It is worth mentioning that the Cs_2NaBiI_6 film shows a narrow distribution of all parameters, which reveals the high uniformity of the vacuum deposition technology. However, the distributions of all parameters become broader after post-treatment, especially after the IPA + DMF process; the reason might be due to the fact that soaking and spinning out of IPA during the IPA treatment process could induce inhomogeneity on the film morphology to certain extent.

Furthermore, the stability of the device is studied. Under continuous 1 sun illumination, the stabilized maximum power output measured at a bias of 0.41 V shows that the current density drops within 10 s and then gradually decreases to \approx 80% of its initial value (**Figure 6a**). This decrease might originate from the increased charge recombination rate when large amount of carriers aggregated at the interfaces under continuous illumination, which is the same reason of the hysteresis effect observed in Figure 4f. Notably, due to the superior stability of Cs₂NaBiI₆, the PSC devices show promising stability in ambient condition (relative humidity (RH) \approx 40%) (Figure 6b). A slight increase in PCE is observed after 100 day, which is mainly caused by the slightly increased $V_{\rm OC}$ (Figure S4, Supporting Information).

The role of the post-treatment process on the photovoltaic performance of Cs₂NaBiI₆-based PSCs is further investigated by carrying out electrochemical impedance spectroscopy (EIS) measurement to describe the charge transfer process in the device. As shown in **Figure 7**a, the Nyquist plot can be used to distinguish the charge transfer/transport at the Cs₂NaBiI₆/Spiro-OMeTAD interface and the charge recombination at the *c*-TiO₂/Cs₂NaBiI₆ interface, and a simplified circuit model is shown in the inset of Figure 7a. [44] In this equivalent circuit diagram, a high-frequency arc is assigned to the diffusion of holes through the hole-transporting material (HTM) Spiro-OMeTAD, which is modeled by an HTM resistance, *R*_{HTM}.

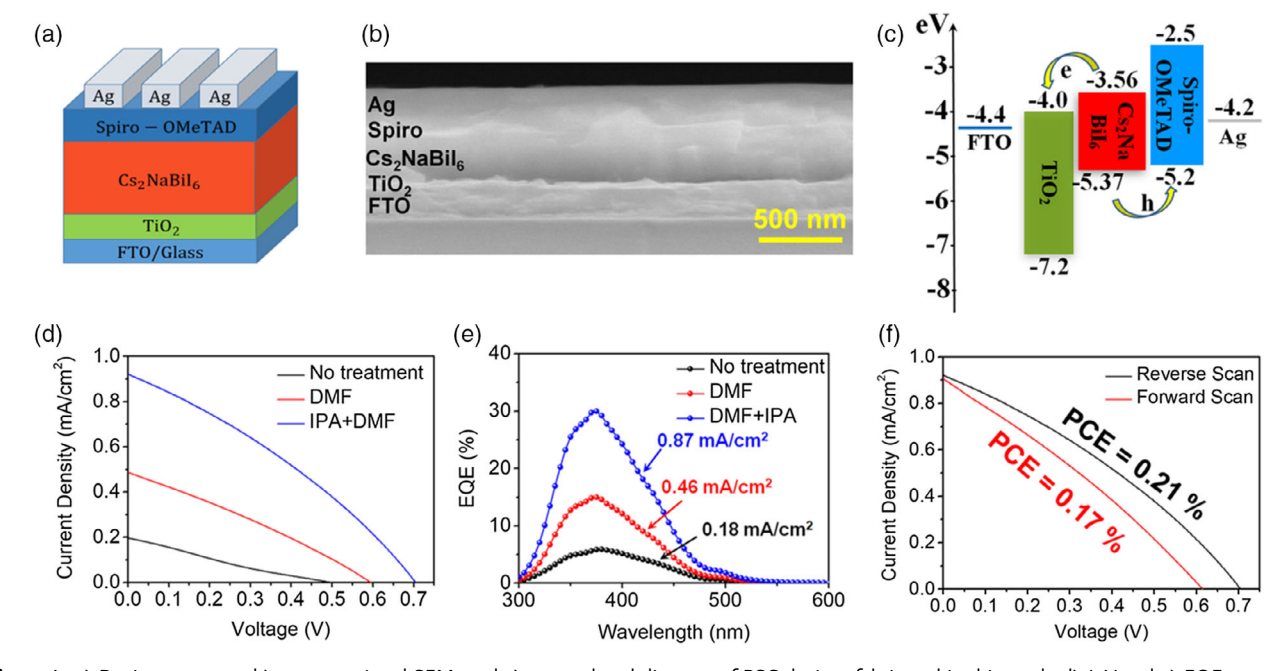


Figure 4. a) Device structure, b) cross-sectional SEM, and c) energy band diagram of PSC devices fabricated in this work. d) J-V and e) EQE measurements of PSC devices based on Cs_2NaBil_6 films with different post-treatment paths. f) The champion device under reverse and forward scan.

18626319, 2019, 23, Downloaded from https://onlinelibrary.wiley.com/doi/10.1002/pssa.201900567 by CAS-XIAN INSTITUTION OPTICS PRECISION MECHANICS, Wiley Online Library on [10/1/12025]. See the Terms

governed by the applicable Creative Commons License

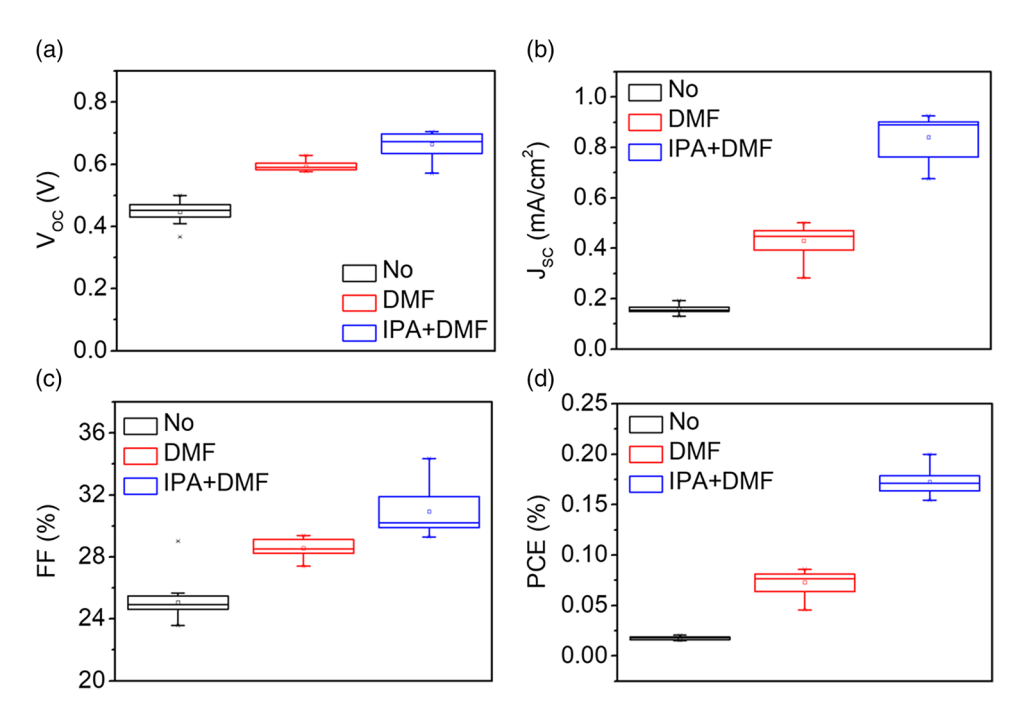


Figure 5. Statistics of the a) V_{OC} , b) J_{SC} , c) FF, and d) PCE distribution of PSCs based on different Cs₂NaBil₆ films. Data are based on 18 individual devices.

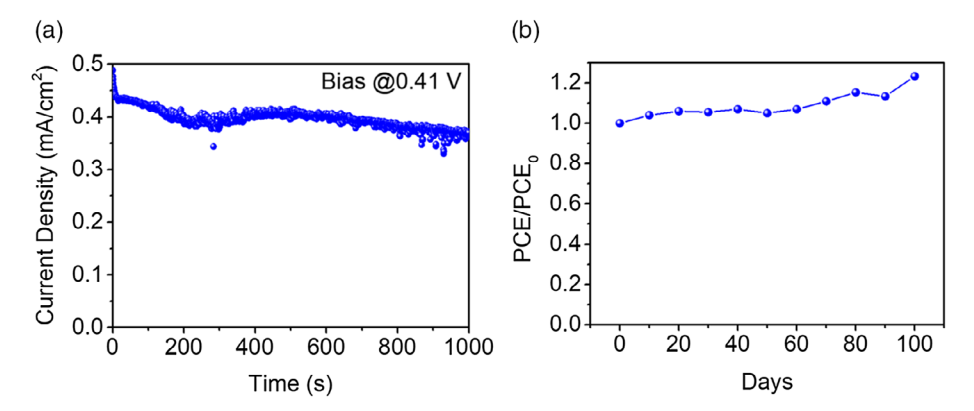


Figure 6. a) Stabilized power output measured at 1 sun illumination conditions in air of the champion PSCs. b) The long-term stability test of PSC devices stored in ambient condition (RH \approx 40%).

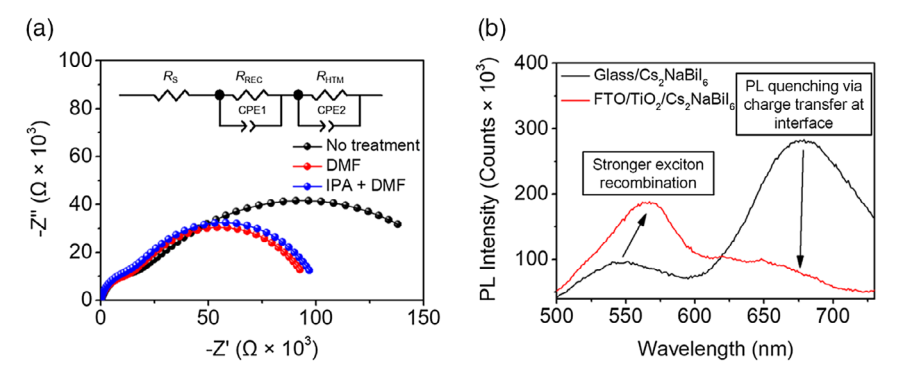


Figure 7. a) EIS measurement of different Cs₂NaBil₆ films. b) PL spectra of the Cs₂NaBil₆ film under different substrates.

18626319, 2019, 23, Downloaded from https://onlineit/brary.wiley.com/doi/10.1002/pssa.201900567 by CAS-XIAN INSTITUTION OPTICS PRECISION MECHANICS, Wiley Online Library on [10/1/12025]. See the Terms and Conditions (https://onlineit/brary.wiley.com/emrs-

and-conditions) on Wiley Online Library for rules of use; OA articles are governed by the applicable Creative Commons License

www.advancedsciencenews.com

Table 1. Fitting results from Nyquist plot of different Cs₂NaBil₆ films.

Sample	$R_{REC} [k\Omega]$	$R_{HTM} [k\Omega]$
No treatment	11.75	119.18
DMF	12.11	83.24
IPA + DMF	12.49	81.77

The lower frequency arc is related to the recombination resistance, $R_{\rm REC}$, which is attributed to the recombination of the electrons with holes at the $c\text{-TiO}_2/\mathrm{Cs}_2\mathrm{NaBiI}_6$ interface. The EIS measurement is conducted under 1 sun illumination under 0 V bias, and **Table 1** collects the fitting results of both resistance values of different $\mathrm{Cs}_2\mathrm{NaBiI}_6$ films. It can be observed that R_{REC} shows a slight increase from 11.75 to 12.49 k Ω after post-treatment of IPA + DMF, indicating an enhanced recombination resistance at the $c\text{-TiO}_2/\mathrm{Cs}_2\mathrm{NaBiI}_6$ interface. At the same time, R_{HTM} decreases from 119.18 to 81.77 k Ω after post-treatment of IPA + DMF, suggesting a reduced charge diffusion resistance at the $\mathrm{Cs}_2\mathrm{NaBiI}_6/\mathrm{Spiro-OMeTAD}$ interface. As a result, the charge transfer/transport at both interfaces becomes more effective after post-treatment, which explains the improved photovoltaic performance of the $\mathrm{Cs}_2\mathrm{NaBiI}_6$ film after the post-treatment process.

It can be seen that after post-treatment, although the parameters of PSC devices all improved after post-treatment, the FF of the device is still poor (\approx 0.34) even under careful parameter optimization (Figure S5, Supporting Information), which hinders the gain of higher PCE. Normally, the poor FF is associated with the interface recombination at the interfaces of PSC devices. To study the charge behavior at the c-TiO₂/Cs₂NaBiI₆ interface, PL spectra of the Cs₂NaBiI₆ film with and without c-TiO₂ layer are measured, as shown in Figure 7b. The PL emission at 675 nm is completely quenched when the c-TiO₂ layer is applied, indicating the efficient transfer of free charge at this interface. However, the exciton PL emission at 550 nm significantly increases when the c-TiO₂ layer is applied, revealing the higher exciton recombination rate at the interface. For double perovskite materials, it has been found that excitonic effects and electron-phonon coupling are their intrinsic characteristics, which could induce unwanted electron-hole recombination and hamper carrier transport. [45] Also, the presence of the c-TiO₂ layer could somehow enhance this excitonic effects and electron-phonon coupling phenomenon. Therefore, such effects might be the reason that leads to the poor FF of Cs2NaBiI6-based PSCs. To solve this problem, doping Cs₂NaBiI₆ and/or modifying the c-TiO₂/Cs₂NaBiI₆ interface could be promising strategies to reduce exciton binding energy of the material.

3. Conclusion

In summary, the high quality of the lead-free Cs_2NaBiI_6 double perovskite film is achieved by vacuum evaporation and post-treatment engineering. This method is valid in enlarging grain size, lowering trap-state density, and removing side product of the Cs_2NaBiI_6 film. As a result, compared with the control device, the Cs_2NaBiI_6 -based PSC devices with optimized post-treatment of IPA soaking and DMF annealing show a tenfold improvement

in PCE (from 0.02% to 0.21%). Moreover, Cs_2NaBiI_6 -based PSC devices show no PCE loss after 100 day storing in ambient condition (RH = 40%). This work demonstrates a universal and robust film deposition strategy to fabricate all inorganic lead-free double perovskite films. The realization of the high-quality double perovskite film could open up new avenue for the efficient lead-free PSC devices and also expand the application field of such material in the future.

Supporting Information

Supporting Information is available from the Wiley Online Library or from the author.

Acknowledgements

This work was financially supported by the National Natural Science Foundation of China (Grant Nos. 11574248, 61875161, 61935016, and 51802253), the China Postdoctoral Science Foundation (Grant Nos. 2018M643649 and 2017M613137), the Fundamental Research Funds for the Central Universities (Grant No. xjj2018018), the National Natural Science Foundation of China (Grant No. 61505161), the Natural Science Basic Research Plan of Shaanxi Province (Grant No. 2017JM6064), and the Scientific Research Plan Projects of Shaanxi Education Department (Grant No. 17JK0700). The SEM and transmission electron microscope work was done at the International Center for Dielectric Research (ICDR), Xi'an Jiaotong University, Xi'an, China.

Conflict of Interest

The authors declare no conflict of interest.

Keywords

double perovskite, post-treatment engineering, solar cells, vacuum deposition

Received: July 8, 2019 Revised: August 22, 2019 Published online: October 21, 2019

- [1] A. Kojima, K. Teshima, Y. Shirai, T. Miyasaka, *J. Am. Chem. Soc.* **2009**, *131*, 6050.
- [2] D. Zhao, C. Wang, Z. Song, Y. Yu, C. Chen, X. Zhao, K. Zhu, Y. Yan, ACS Energy Lett. 2018, 3, 305.
- [3] J. Xi, K. Xi, A. Sadhanala, K. H. Zhang, G. Li, H. Dong, T. Lei, F. Yuan, C. Ran, B. Jiao, *Nano Energy* **2019**, *56*, 741.
- [4] H. Dong, J. Xi, L. Zuo, J. Li, Y. Yang, D. Wang, Y. Yu, L. Ma, C. Ran, W. Gao, Adv. Funct. Mater. 2019, 29, 1808119.
- [5] J. Dai, J. Xi, L. Li, J. Zhao, Y. Shi, W. Zhang, C. Ran, B. Jiao, X. Hou, X. Duan, Angew. Chem., Int. Ed. 2018, 57, 5754.
- [6] F. Wei, B. Jiao, J. Xu, T. Lei, Y. Yu, L. Ma, J. Zhang, D. Wang, J. Chen, X. Hou, J. Mater. Chem. A, 2019, https://doi.org/10.1039/ C9TA03898A.
- [7] F. Igbari, Z. K. Wang, L. S. Liao, Adv. Energy Mater. 2019, 9, 1803150.
- [8] A. Babayigit, A. Ethirajan, M. Muller, B. Conings, Nat. Mater. 2016, 15, 247

18526319, 2019, 23, Dowlooaded from https://onlinelibrary.wiley.com/doi/10.1002/pss.20.1900567 by CAS-XIAN INSTITUTION OPTICS PRECISION MECHANICS, Wiley Online Library on [10/11/2025]. See the Terms

governed by the applicable Creative Commons I

www advancedsciencenews com

- [9] T. A. Berhe, W.-N. Su, C.-H. Chen, C.-J. Pan, J.-H. Cheng, H.-M. Chen, M.-C. Tsai, L.-Y. Chen, A. A. Dubale, B.-J. Hwang, *Energy Environ. Sci.* 2016, 9, 323.
- [10] T. Leijtens, G. E. Eperon, N. K. Noel, S. N. Habisreutinger, A. Petrozza, H. J. Snaith, Adv. Energy Mater. 2015, 5, 1500963.
- [11] Z. Shi, J. Guo, Y. Chen, Q. Li, Y. Pan, H. Zhang, Y. Xia, W. Huang, Adv. Mater. 2017, 29, 1605005.
- [12] Z. Xiao, Z. Song, Y. Yan, Adv. Mater. 2019, 31, 1803792.
- [13] N. K. Noel, S. D. Stranks, A. Abate, C. Wehrenfennig, S. Guarnera, A.-A. Haghighirad, A. Sadhanala, G. E. Eperon, S. K. Pathak, M. B. Johnston, *Energy Environ. Sci.* 2014, 7, 3061.
- [14] S. Shao, J. Liu, G. Portale, H.-H. Fang, G. R. Blake, G. H. ten Brink, L. J. A. Koster, M. A. Loi, Adv. Energy Mater. 2018, 8, 1702019.
- [15] J. Xi, Z. Wu, B. Jiao, H. Dong, C. Ran, C. Piao, T. Lei, T. B. Song, W. Ke, T. Yokoyama, Adv. Mater. 2017, 29, 1606964.
- [16] F. Hao, C. C. Stoumpos, D. H. Cao, R. P. Chang, M. G. Kanatzidis, Nat. Photonics 2014, 8, 489.
- [17] T. Krishnamoorthy, H. Ding, C. Yan, W. L. Leong, T. Baikie, Z. Zhang, M. Sherburne, S. Li, M. Asta, N. Mathews, J. Mater. Chem. A 2015, 3, 23829
- [18] I. Kopacic, B. Friesenbichler, S. F. Hoefler, B. Kunert, H. Plank, T. Rath, G. Trimmel, ACS Appl. Energy Mater. 2018, 1, 343.
- [19] Z. Yi, N. H. Ladi, X. Shai, H. Li, Y. Shen, M. Wang, Nanoscale Adv. 2019. 1, 1276.
- [20] X. X. Ma, Z. S. Li, Phys. Status Solidi B 2019, 256, 1800427.
- [21] B. Saparov, F. Hong, J.-P. Sun, H.-S. Duan, W. Meng, S. Cameron, I. G. Hill, Y. Yan, D. B. Mitzi, Chem. Mater. 2015, 27, 5622
- [22] X.-G. Zhao, D. Yang, J.-C. Ren, Y. Sun, Z. Xiao, L. Zhang, Joule 2018, 2, 1662.
- [23] Z. Li, Q. Xu, Q. Sun, Z. Hou, W.-J. Yin, Adv. Funct. Mater. 2019, 29, 1807280.
- [24] X.-G. Zhao, J.-H. Yang, Y. Fu, D. Yang, Q. Xu, L. Yu, S.-H. Wei, L. Zhang, J. Am. Chem. Soc. 2017, 139, 2630.
- [25] E. T. McClure, M. R. Ball, W. Windl, P. M. Woodward, Chem. Mater. 2016, 28, 1348.
- [26] T. T. Tran, J. R. Panella, J. R. Chamorro, J. R. Morey, T. M. McQueen, Mater. Horiz. 2017, 4, 688.

- [27] F. Wei, Z. Deng, S. Sun, F. Zhang, D. M. Evans, G. Kieslich, S. Tominaka, M. A. Carpenter, J. Zhang, P. D. Bristowe, *Chem. Mater.* 2017, 29, 1089.
- [28] F. Wei, Z. Deng, S. Sun, F. Xie, G. Kieslich, D. M. Evans, M. A. Carpenter, P. D. Bristowe, A. K. Cheetham, *Mater. Horiz.* 2016, 3, 328.
- [29] Z. Deng, F. Wei, S. Sun, G. Kieslich, A. K. Cheetham, P. D. Bristowe, J. Mater. Chem. A 2016, 4, 12025.
- [30] C. Zhang, L. Gao, S. Teo, Z. Guo, Z. Xu, S. Zhao, T. Ma, Sustainable Energy Fuels 2018. 2. 2419.
- [31] W. Gao, C. Ran, J. Xi, B. Jiao, W. Zhang, M. Wu, X. Hou, Z. Wu, ChemPhysChem 2018, 19, 1696.
- [32] E. Greul, M. L. Petrus, A. Binek, P. Docampo, T. Bein, J. Mater. Chem. A 2017, 5, 19972.
- [33] C. Wu, Q. Zhang, Y. Liu, W. Luo, X. Guo, Z. Huang, H. Ting, W. Sun, X. Zhong, S. Wei, Adv. Sci. 2018, 5, 1700759.
- [34] M. Wang, P. Zeng, S. Bai, J. Gu, F. Li, Z. Yang, M. Liu, Sol. RRL 2018, 2, 1800217.
- [35] M. Pantaler, C. Fettkenhauer, H. L. Nguyen, I. Anusca, D. C. Lupascu, MRS Adv. 2018, 3, 1819.
- [36] H. Lan, C. Lan, G. Liang, J. Luo, X. Ma, P. Fan, J. Mater. Sci.: Mater. Electron. 2018, 29, 2267.
- [37] G. Tong, H. Li, G. Li, T. Zhang, C. Li, L. Yu, J. Xu, Y. Jiang, Y. Shi, K. Chen, Nano Energy 2018, 48, 536.
- [38] M. Lyu, J.-H. Yun, M. Cai, Y. Jiao, P. V. Bernhardt, M. Zhang, Q. Wang, A. Du, H. Wang, G. Liu, *Nano Res.* 2016, 9, 692.
- [39] N. Wang, Y. Zhou, M. G. Ju, H. F. Garces, T. Ding, S. Pang, X. C. Zeng, N. P. Padture, X. W. Sun, Adv. Energy Mater. 2016, 6, 1601130.
- [40] C. Ran, J. Xu, W. Gao, C. Huang, S. Dou, Chem. Soc. Rev. 2018, 47, 4581.
- [41] C. Ran, W. Gao, N. Li, Y. Xia, Q. Li, Z. Wu, H. Zhou, Y. Chen, M. Wang, W. Huang, ACS Energy Lett. 2018, 4, 358.
- [42] A. H. Slavney, T. Hu, A. M. Lindenberg, H. I. Karunadasa, J. Am. Chem. Soc. 2016, 138, 2138.
- [43] B. Chen, M. Yang, S. Priya, K. Zhu, J. Phys. Chem. Lett. 2016, 7, 905.
- [44] D. S. Lee, W. Kim, B. G. Cha, J. Kwon, S. J. Kim, M. Kim, J. Kim, D. H. Wang, J. H. Park, ACS Appl. Mater. Interfaces 2015, 8, 449.
- [45] R. Kentsch, M. Scholz, J. Horn, D. Schlettwein, K. Oum, T. Lenzer, J. Phys. Chem. C 2018, 122, 25940.